Impact of Orographic Gravity Wave Drag Parameterization on Northeast China Cold Vortex Heavy Rainfall Simulated at a Convection-Allowing Resolution

MINGSHAN LI,[a,b,c] XIN XU,[b,c,d] MING XUE,[e] ZHENZHEN AI,[b,c,d] KEFENG ZHU,[f] AND SHANGFENG LI[g]

[a] *Jingmen Meteorological Service, Jingmen, China*
[b] *State Key Laboratory of Severe Weather Meteorological Science and Technology, Nanjing University, Nanjing, China*
[c] *Key Laboratory of Mesoscale Severe Weather/Ministry of Education and School of Atmospheric Sciences, Nanjing University, Nanjing, China*
[d] *Key Laboratory of Radar Meteorology, China Meteorology Administration, Nanjing, China*
[e] *Center for Analysis and Prediction of Storms and School of Meteorology, University of Oklahoma, Norman, Oklahoma*
[f] *Nanjing Innovation Institute for Atmospheric Sciences, Chinese Academy of Meteorological Sciences–Jiangsu Meteorological Service, Nanjing, China*
[g] *Jilin Provincial Key Laboratory of Changbai Mountain Meteorology and Climate Change, Laboratory of Research for Middle-High Latitude Circulation Systems and East Asian Monsoon, Institute of Meteorological Sciences of Jilin Province, Changchun, China*

(Manuscript received 27 February 2025, in final form 19 July 2025, accepted 30 September 2025)

ABSTRACT: The Northeast China cold vortex (NECV) is a major weather system producing heavy rainfall in northern China, yet the influence of complex terrain, especially orographic gravity waves (OGWs), on such heavy rainfall remains poorly understood. This study investigates the impact of OGW drag (OGWD) parameterization on an NECV heavy rainfall event over the southern Yanshan Mountains on 6 July 2011, using the Weather Research and Forecasting Model at 3-km resolution. Results show that the OGWD parameterization can weaken the NECV circulation and diminish the orographic lifting and moisture transport over the southern slope of the Yanshan Mountains given the decelerated upslope flow. Therefore, the overestimation of the heavy rainfall intensity in the absence of OGWD parameterization was alleviated significantly, indicating the importance of OGWD parameterization even in high-resolution numerical models. However, the parameterization of OGWD introduced weak but widespread spurious rainfall ahead of the Taihang Mountains, as it decelerated the northwesterly downslope winds on the southeastern slope of the Taihang Mountains which enhanced the upslope moisture transport. This spurious rainfall was mitigated significantly when using a revised OGWD scheme accounting for the nonhydrostatic effect (NHE) on the surface momentum flux of vertically propagating OGWs. The NHE more notably attenuated the OGWD over the Taihang Mountains than over the Yanshan Mountains, which strengthened the NECV northwesterly flow downgliding the Taihang Mountains and inhibited the moisture transport.

KEYWORDS: Cutoff lows; Rainfall; Numerical weather prediction/forecasting; Parameterization; Subgrid-scale processes

1. Introduction

Synoptic-scale cutoff lows (COLs) originating from the polar region are often observed in Northeast China (Zheng et al. 1992; Nieto et al. 2005), which are commonly referred to as Northeast China cold vortices (NECVs). NECV is a prominent weather system in Northeast China which affects about half of the summer precipitation and often causes flooding, resulting in severe fatalities and economic losses (Sun 1997; Zhao and Sun 2007; Hu et al. 2010; Xu et al. 2023). The NECVs can also promote severe convective weather like hail, high winds, and tornadoes (Luo et al. 2020; Wu et al. 2021; Yin et al. 2021; Li et al. 2021; Meng et al. 2018). For example, more than 50% (53%) of thunderstorm winds (warm season hail) and ~28% of overshooting convection in Northeast China are closely associated with NECVs (Zhang et al. 2008; Liu and Liu 2018). Yang and Zheng (2024) studied the climatological characteristics of short-duration heavy rainfall events in Northeast China and found that ~40% were attributed to NECVs, with the southeast quadrant of NECV featured by strong intensity, frequent occurrence, and long duration rainfall. Chen et al. (2023) found that the heavy rainfall is mostly concentrated within 2000-km radius in the southeast quadrant of NECVs.

The NECV-induced heavy rainfall is usually related to high atmospheric baroclinity, strong flow convergence, and rich water vapor (Zhao and Sun 2007; Liu and Liu 2018). Dry invasion of the NECV in conjunction with northward-moving tropical systems that transport water vapor is conducive to the onset of conditional instability, creating an environment favorable for heavy rainfall (Zhong et al. 2015; Liu et al. 2017; Luo et al. 2020; Liu et al. 2024). Wang et al. (2021) analyzed an extreme rainfall event in Northeast China from multiscale perspective. They found that a mesoscale convergence line played an important role in triggering the convection, and convective echo training was responsible for the persistence of the extreme rainfall at night.

In addition to the aforementioned multiscale weather systems, there is complex terrain in North and Northeast China (Fig. 1), the impact of which on the NECV-induced heavy rainfall is rarely examined in the literature. Indeed, the importance of underlying terrain in the formation of heavy rainfall has been well recognized (see Houze 2012 and references therein), especially in North China (e.g., Zhang et al. 2013; Xia and Zhang 2019; Wei et al. 2023; Wei et al. 2025) and

Corresponding author: Xin Xu, xinxu@nju.edu.cn

DOI: 10.1175/MWR-D-25-0037.1

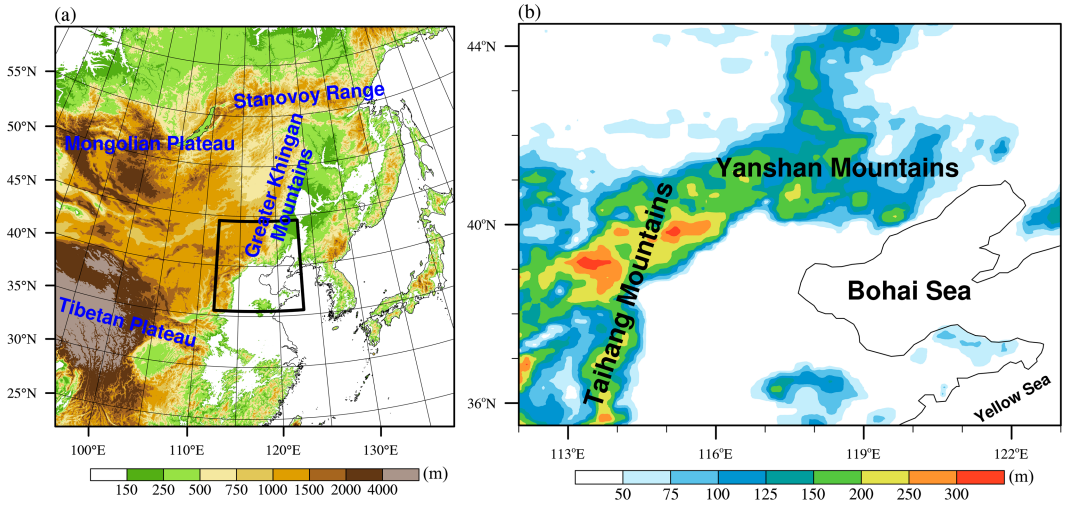

FIG. 1. (a) Model domain and resolved orography (shading; m). (b) Standard deviation of the subgrid-scale orography height (shading; m) in the region outlined in black in (a). Note that the thin black solid lines in (b) near the Bohai Sea indicate the coastline.

South China (e.g., Zhang et al. 2020; Du et al. 2021; Zhang et al. 2024). Zhong et al. (2015) investigated a warm-sector heavy rainfall in Beijing, North China. They found that the moist airflow carried by low-level jet (LLJ) could be lifted on the mountain windward slope to produce heavy precipitation. Hua et al. (2020) studied the influence of multiscale orography on the initiation and maintenance of a heavy rainfall-producing convective system over the Taihang Mountains in North China. The low-level convergence at the mountain top was enhanced by a localized mountain–plains solenoid circulation due to the solar radiative heating, which finally led to convection initiation. Du et al. (2021) examined the convection initiation of a heavy rainfall event at the coast of South China. The concave coastal terrain acted as a local moisture catcher that promoted low-level moistening by blocking the water vapor from the ocean.

Besides mechanical uplifting, thermal forcing, and moistening, small-scale complex terrain can trigger orographic gravity waves (OGWs), the breaking of which can decelerate the ambient flow via momentum deposition, i.e., OGW drag (OGWD) (e.g., Smith 1979; Teixeira 2014). This drag force caused by small-scale orography often needs to be parameterized in numerical models because it cannot be fully resolved by the model grid (e.g., Kim et al. 2003; Sandu et al. 2019). Previous studies had shown great importance of OGWD on the weather and climate systems at both global and regional scales, such as the mesospheric circulation, polar vortex, and Asian monsoon rainfall (Kim 2007; McLandress et al. 2012; Sandu et al. 2016; Zhou et al. 2017; Zhang et al. 2020; White et al. 2021; Li et al. 2023). Recently, Xu et al. (2023a) studied the impact of OGWD on the intensity of an NECV based on numerical simulations using the Weather Research and Forecasting (WRF) Model (Skamarock et al. 2019). The OGWD directly weakened the low-level convergence of the NECV, inducing an anticyclonic circulation which indirectly weakened the NECV in the mid–upper troposphere by suppressing posttrough cold advection. This NECV also produced heavy rainfall over complex terrain (see section 3) which, however, was not studied in Xu et al. (2023a).

The first purpose of this work is thus to examine the impact of OGWD on the heavy rainfall produced by that NECV. Note that the WRF simulations in Xu et al. (2023a) adopted a relatively coarse resolution of 27 km which was insufficient to resolve the synoptic NECV and embedded precipitation. To better capture heavy rainfall, a grid spacing of 3 km or smaller is needed (e.g., Fan et al. 2024). At such resolutions, the OGWD is often believed to be well resolved by the fine grid and there is no need for OGWD parameterization (Sandu et al. 2019). However, the observational and modeling studies of Kruse et al. (2022) argue that small-scale OGWs are underresolved or overdiffused even at 3-km grid spacing. Thus, the need for parameterization of OGWD in high-resolution models remains in debate, and this study tries to determine the effects of OGWD parameterization on NECV precipitation when simulated at 3-km grid spacing.

The second purpose of this work is to evaluate the performance of a newly developed OGWD parameterization scheme for the simulation of heavy rainfall. Historically, OGWD parameterization schemes are developed for coarse-resolution models, the subgrid-scale orography (SSO) considered within is in general broad in scale, and the corresponding OGWs are in hydrostatic balance (Smith 1980; Lott and Miller 1997). The SSO becomes more and more narrow in scale as the model resolution increases, which will support nonhydrostatic OGWs (e.g., Xue and Thorpe 1991). Xu et al. (2021) theoretically derived the asymptotic solution for three-dimensional OGWs which has been used to revise traditional OGWD schemes. The revised scheme accounts for the nonhydrostatic effect (NHE) on the momentum flux of vertically propagating OGWs and has been implemented in the Model for Prediction Across Scales (MPAS; Skamarock et al. 2012) and the WRF Model, improving the simulations of polar night jet in the Northern Hemisphere, winter precipitation over the western Tibetan Plateau, and the NECV intensity (Xu et al. 2023b; Xu et al. 2024; M. Li et al. 2024). Herein, the scheme is further

evaluated for the short-range forecast of rainfall, taking the heavy rainfall produced by an NECV as an example.

The rest of the paper is organized as follows. Section 2 describes the datasets and setup of numerical experiments. The environmental conditions of the NECV-induced heavy rainfall are analyzed in section 3. The model results are presented in section 4, with focus on the impacts of parameterized OGWD on the simulation of heavy rainfall. Finally, the paper is summarized and discussed in section 5.

2. Datasets and numerical experiments

The ERA5 reanalysis data of the European Centre for Medium-Range Weather Forecasts (ECMWF) (Hersbach et al. 2018), which has a horizontal resolution of 0.25° and time interval of 1 h, are used to study the evolution of the NECV of interest and provide the initial and boundary conditions for the numerical experiments with the WRF v4.2.1 Model. Moreover, half hourly, 0.1° precipitation of Integrated Multi-satellitE Retrievals for Global Precipitation Measurement (IMERG; Huffman et al. 2023) is used for verification.

The NECV case is simulated using the WRF v4.2.1 Model, with the model domain and unresolved orography, i.e., SSO, given in Figs. 1a and 1b, respectively. The horizontal grid spacing is 3 km, along with 39 levels in the vertical. The model top is placed at 50 hPa, accompanied by a Rayleigh damping layer at the topmost 5 km to prevent artificial gravity wave reflection at the model top. The model physics used are the new Thompson microphysics scheme (Thompson et al. 2008), the Rapid Radiative Transfer Model for general circulation models (RRTMG) longwave and shortwave radiation schemes (Iacono et al. 2008), the Fifth-generation Pennsylvania State University–National Center for Atmospheric Research Mesoscale Model (MM5) similarity scheme for the surface layer (Beljaars 1995), the Noah land surface model (Tewari et al. 2004), and the Yonsei University planetary boundary layer scheme (Hong et al. 2006). The parameterization of cumulus convection is turned off.

Three numerical experiments are conducted, i.e., EXP_NoGWD, EXP_KD05, and EXP_X21, respectively. In the first one, the parameterization of OGWD is turned off. In the latter two experiments, we use the original and revised parameterization schemes of OGWD, respectively. The original scheme was developed by Kim and Doyle (2005, hereafter KD05), whereas the revised one adds the NHE effect to the original scheme based on solutions derived in Xu et al. (2021, hereafter X21), and the NHE tends to weaken the OGWD. Details of the OGWD schemes can be found in appendix A. Comparison between EXP_NoGWD and EXP_KD05 serves to reveal the impact of OGWD on the heavy rainfall, while the performance of the revised OGWD scheme is evaluated by comparing EXP_X21 and EXP_KD05. All three numerical experiments start from 0000 UTC 6 July and are integrated for 24 h until 0000 UTC 7 July 2011. The first 6 h are taken as the model spinup period.

3. Case overview

The NECV in question moved to the vicinity of the Greater Khingan Mountains (Fig. 1a) at 1200 UTC 6 July, with the minimum 500-hPa geopotential height (GPH) as low as 5517 gpm (Fig. 2a; near 118°E and 48°N). A distinct cold core was found west of the vortex center, indicating strong cold air advection which favored the deepening of the NECV. The heavy rainfall area is located ahead of the midtropospheric trough, which extended southwestward from the NECV center to western Inner Mongolia. The 200-hPa upper-level jet stream was located south of the NECV, with the maximum wind speed exceeding 60 m s^{-1}. At 925 hPa (Fig. 2b), there was a southwesterly LLJ of over 16 m s^{-1} stretching from about 42°N, 122°E to 46°N, 127°E. The heavy rainfall occurred upstream of the LLJ where the low-level convergence was weak. Nonetheless, as will be shown below, the underlying terrain (Fig. 3a) can provide the dynamical lifting for the generation of heavy rainfall.

The heavy rainfall [i.e., the maximum accumulated rainfall was 47.6 mm $(6\ h)^{-1}$, see below] was fed by plentiful moisture from the nearby Bohai Sea. Figure 2c displays the distribution of layer-averaged specific humidity between the surface and 700 hPa. In general, the eastern/southeastern part of the NECV was characterized by high humidity, with the maximum layer-averaged specific humidity between the surface and 700 hPa exceeding 13 g kg^{-1}. This is due to the presence of the LLJ which transported abundant water vapor from the Bohai Sea and Yellow Sea. The heavy rainfall was in close proximity to the center of averaged moisture of over 12 g kg^{-1}, indicating sufficient water vapor supply.

Figure 2d shows an atmospheric sounding extracted from the ERA5 reanalysis at 1200 UTC 6 July 2011 (i.e., about 3 h before the heavy rainfall). The sounding was averaged within a 1° × 1° box encompassing the rainfall center. The dewpoint depression in the lower troposphere below 800 hPa was about 2–3 K, indicating good humidity condition, given the moisture transport by the low-level southwesterly jet. In contrast, the dewpoint depression in the mid- and upper troposphere exceeded 10 K which was due to the intrusion of the posttrough cold, dry northwesterly flow. Such lower-wet and upper-dry air masses created an unstable layer of moderate convective available potential energy (CAPE) of 695 J kg^{-1}, which increased to 1029 J kg^{-1} at 1600 UTC. The lifting condensation level (LCL) and the level of free convection (LFC) were as low as 880 and 1589 m, respectively. The heavy rainfall occurred on the windward slope of the Yanshan Mountains (see geography in Fig. 1) where the terrain elevation is over 1000 m (Fig. 3a). The orographic upslope lifting is sufficient to lift the air parcel to the LCL, promoting rainfall. Note that due to the coarse vertical/horizontal resolution and the lack of explicit convection, the ERA5 reanalysis may underestimate the metrics such as CAPE and LCL.

From the above analyses, the heavy rainfall developed in an environment of rich moisture, favorable dynamical forcing of the NECV and mechanical lifting of the underlying terrain. The rainfall center was located on the southeastern slope of the Yanshan Mountains (Fig. 3a). This nocturnal rainfall was short lived which began from about 1500 UTC (2300 LST) 6 July and dissipated around 0200 UTC (1000 LST) 7 July 2011 (Fig. 3b). The most intense rainfall occurred between 1800 UTC 6 July and 0000 UTC 7 July,

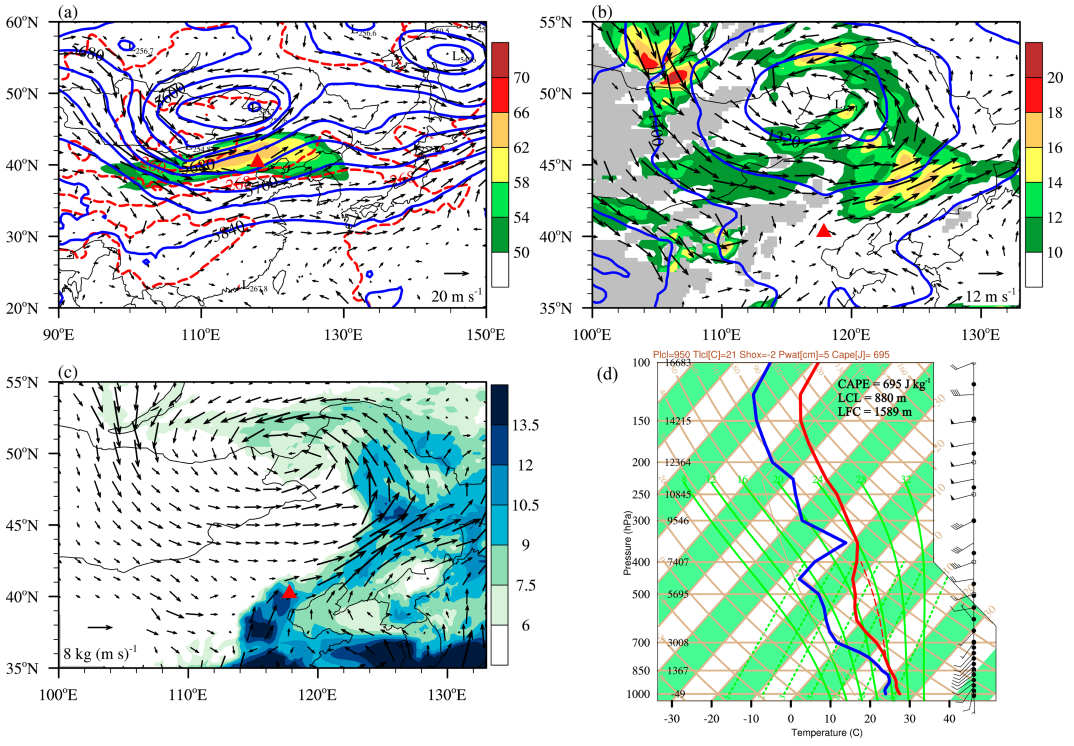

FIG. 2. (a) GPH (blue contours at an interval of 40 gpm; gpm), temperature (red contours at an interval of 4 K; K), and horizontal wind (vector; m s^{-1}) at 500 hPa and horizontal wind speed (shaded; m s^{-1}) at 200 hPa; (b) GPH (blue contour; gpm) and horizontal wind (vector; m s^{-1}) and its speed (shaded; m s^{-1}) at 925 hPa; and (c) layer-averaged horizontal WVF (vector; kg m^{-1} s^{-1} Pa^{-1}) and specific humidity (shaded; g kg^{-1}) between the surface and 700 hPa obtained from the ERA5 reanalysis at 1200 UTC 6 Jul 2011. The symbol of solid red triangle in (a)–(c) indicates the location of the rainfall center which is obtained from the IMERG data. The gray area in (b) represents the region underground. (d) Skew *T* diagram for the atmospheric sounding averaged within an area of 1° × 1° centered at the maximum rainfall extracted from the ERA5 reanalysis at 1200 UTC 6 Jul 2011. Red and blue lines represent temperature and dewpoint temperature, respectively. Full (half) wind barb represents 4 m s^{-1} (2 m s^{-1}).

with the hourly rainfall rate reaching 20.7 mm h^{-1} at 2100 UTC. In the next section, we will focus on this 6-h period, during which the maximum accumulated rainfall was 47.6 mm.

4. Results

a. Simulated precipitation and circulation without OGWD parameterization

The spatial distribution of the accumulated precipitation between 1800 UTC 6 July 2011 and 0000 UTC 7 July 2011 in experiment EXP_NoGWD is shown in Fig. 4c (see also Fig. 6a). Overall, the location of the simulated precipitation is consistent with the IMERG data (which was considered as observation). However, the rainfall intensity is notably overestimated by the model, with the maximum value reaching 60.7 mm.

Figures 4a and 4b separately show the horizontal wind and its speed at 925 hPa and the layer-averaged specific humidity vertically integrated from the surface to 700 hPa at 1800 UTC 6 July 2011 based on the ERA5 reanalysis. Unlike that at 1200 UTC, there were two maxima of southwesterly LLJs of over 12 m s^{-1} at 925 hPa, which were in general parallel to the Taihang and Yanshan Mountains, respectively (Fig. 4a). The heavy rainfall was located between the two LLJs, on the windward slope higher than 250 m in elevation. Since the Yanshan Mountains were basically along the west–east direction, the southwesterly flow was largely blocked, leading to relatively low wind speed between the two LLJs. Upstream of the heavy rainfall, there existed an area of high specific humidity of over 12 g kg^{-1} in the lower troposphere (Fig. 4b). The western LLJ continuously transported this abundant moisture downstream which was forced to move upward on the windward slope of the Yanshan Mountains (i.e., orographic mechanical lifting) and eventually led to the formation of heavy rainfall.

Figures 4c and 4d are the same as Figs. 4a and 4b, but for experiment EXP_NoGWD. Without gravity wave drag, the WRF Model can also capture the overall features of the wind circulation (e.g., two LLJs) and moisture transport, especially their locations (Figs. 4c,d), but the intensity of the LLJs is overestimated evidently. For example, the maximum wind speed of the western LLJ exceeds 16 m s^{-1}, and the horizontal winds between the two low-level jets are stronger than 12 m s^{-1} while they are less than 10 m s^{-1} in ERA5 (Fig. 4a). This is due to the fact that the NECV intensity is overestimated in the absence of OGWD parameterization, accompanied with too-low GPH (e.g., the

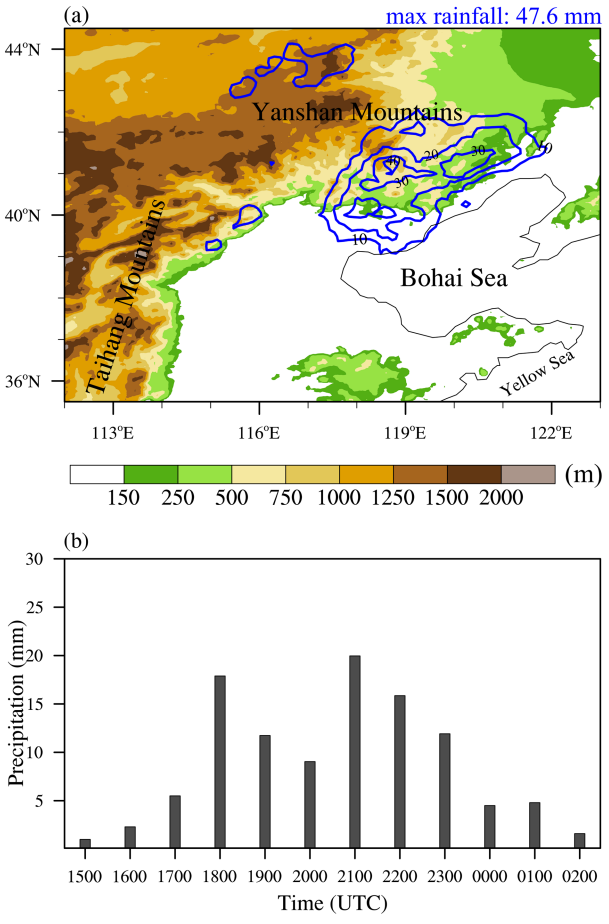

FIG. 3. (a) Geographic distribution of the 6-h accumulative precipitation (contours at an interval of 10 mm; mm), with the maximum rainfall value labeled in the top-right corner, and the model resolved orography (shading; m). The thin black solid line near the Bohai Sea indicates the coastline. (b) Histogram of maximum hourly precipitation (mm h^{-1}) during the period of 1500 UTC 6 Jul 2011–0200 UTC 7 Jul 2011 obtained from the IMERG data.

500-hPa GPH minima of the NECV obtained from ERA5 and EXP_NoGWD experiment are 5503 and 5482 gpm, respectively), and thus overall stronger horizontal winds given the geostrophic balance (Fig. 5). The stronger southwesterly flow transports excessive water vapor to the windward slope of the Yanshan Mountains (Fig. 4d). It also causes stronger uplifting because the orographically forced vertical velocity is proportional to the speed of incoming flow (Smith 1979). Consequently, the heavy rainfall is overestimated in the WRF Model (Figs. 4c,d).

b. *Impact of OGWD on the precipitation and wind circulation*

1) ORIGINAL KD05 SCHEME

In experiment EXP_KD05 using the original OGWD scheme, the overestimation of heavy rainfall intensity is alleviated. As shown in Fig. 6b, the maximum rainfall decreases to 44.6 mm, in better agreement with observation than in EXP_NoGWD (Fig. 6a). Figure 7a shows the differences between the wind circulations at 925 hPa in experiments EXP_KD05 and EXP_NoGWD. Note that the wind fields are smoothed by using two-dimensional fast Fourier transform (FFT) to remove disturbances of horizontal scales less than 150 km for a clearer view. (The unsmoothed wind fields can be found in appendix B.) The wind difference exhibits an anticyclonic circulation which moved downslope of the Yanshan Mountains (see the northwesterly/northerly winds east of 117.5°E) and upslope of the Taihang Mountains (southeasterly winds near 116°E). This is due to the weakening of the NECV by the parameterized OGWD (figure omitted). As shown in Fig. 7b, there is remarkable column-integrated OGWD of larger than 2.0×10^{-3} Pa m s^{-2} over the Taihang Mountains where salient SSO is present (Fig. 1b), while it is much weaker over the Yanshan Mountains. The OGWD is mainly directed toward northwest over the Taihang Mountains and southwest over the Yanshan Mountains, agreeing with the anticyclonic circulation in Fig. 7a. This is because the OGWD is produced as the northwesterly and southwesterly winds of the NECV pass over the Taihang and Yanshan Mountains (see the horizontal wind fields at 925 hPa in Fig. 2b).

In response to the weakened upslope flow over the Yanshan Mountains, both the moisture transport and orographic lifting are suppressed, which are clearly shown in Figs. 8a and 8c. In EXP_NoGWD, there is obvious upward motion of over -4 Pa s^{-1} near the rainfall center at about 40.5°N on the southern slope of the Yanshan Mountains (Fig. 8a) where the low-level southwesterly flow is lifted by the terrain (Fig. 4d). The upslope flow also brings plentiful moisture, with the maximum water vapor flux (WVF) exceeding 9×10^{-2} kg m^{-1} s^{-1} Pa^{-1} at about 750 hPa. In EXP_KD05, the vertical motion near the rainfall center is notably reduced by more than 1.5 Pa s^{-1}, and the WVF is reduced by more than 3×10^{-2} kg m^{-1} s^{-1} Pa^{-1} below 850 hPa (Fig. 8c). The weakened vertical lifting and moisture lead to a decrease of 2 K in equivalent potential temperature below ~900 hPa on the southern slope of the Yanshan Mountains (Fig. 8e), thereby reducing the low-level atmospheric instability there.

On the contrary, the anticyclonic circulation acts to inhibit the downslope flow over the southeastern slope of the Taihang Mountains. In EXP_NoGWD, northerly flow is found over and ahead of the southeastern slope of the Taihang Mountains where the WVF is negative (Fig. 8b). Compared with EXP_NoGWD, EXP_KD05 shows more southerly winds toward the Taihang Mountains which are forced to move upward, resulting in an apparent vertical velocity of over -1.5 Pa s^{-1} around 39.5°N (Fig. 8d). The southerly winds also cause a positive WVF which can exceed 4.5×10^{-2} kg m^{-1} s^{-1} Pa^{-1} ahead of the topography, thus significantly inhibiting the downslope dry air from the north. As a result, the low-level equivalent potential temperature is increased by more than 4 K ahead of the Taihang Mountains (Fig. 8f), indicating enhanced atmospheric instability that contributes to the generation of widespread spurious rainfall (Fig. 6b).

2) REVISED X21 SCHEME

When accounting for the NHE in the KD05 OGWD scheme, the intensity of the heavy rainfall over the southern slope of the

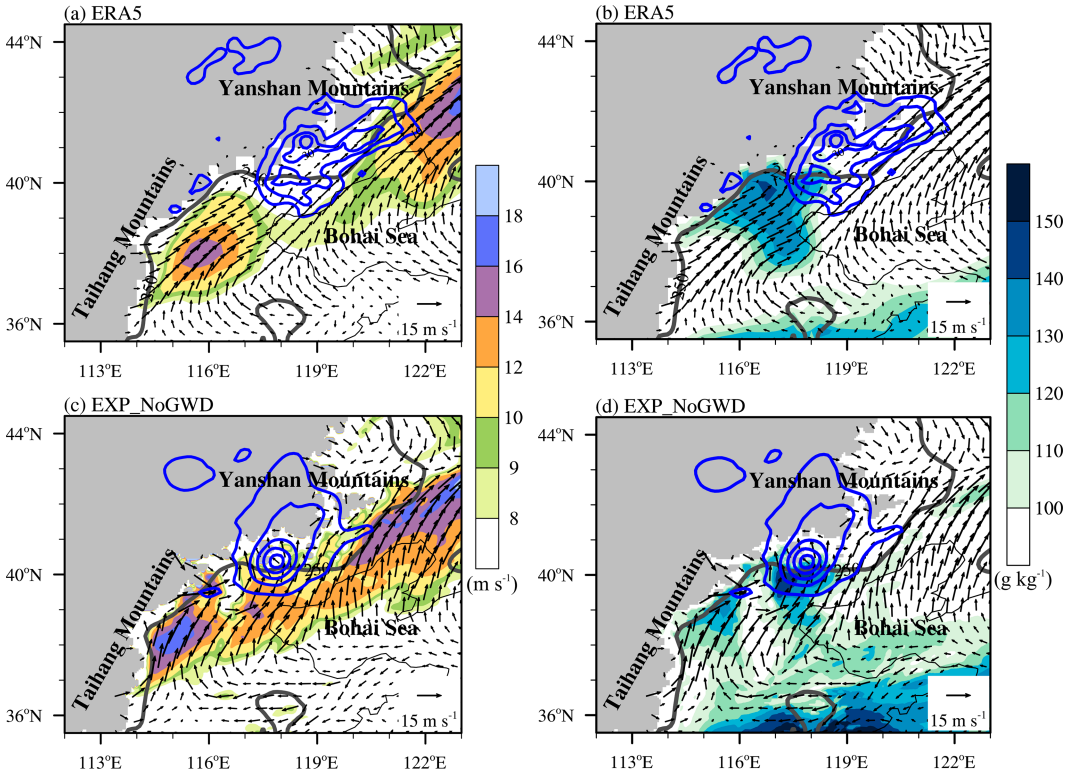

FIG. 4. (a),(c) Horizontal wind speed at 925 hPa (shaded; m s^{-1}) and (b),(d) layer-averaged specific humidity between the surface and 700 hPa (shaded; g kg^{-1}) obtained from ERA5 reanalysis and EXP_NoGWD, respectively, at 1800 UTC 6 Jul 2011. Note that the arrows indicate the 925-hPa wind vector, blue contours are the 6-h accumulated rainfall (contours at an interval of 10 mm; mm), and gray contours denote the terrain elevation of 250 m. Note that the thin black solid lines near the Bohai Sea indicate the coastline.

Yanshan Mountains decreases to 41.7 mm (Fig. 6c), which is a little bit weaker than in EXP_KD05 (Fig. 6b) but still in good agreement with observation. Indeed, the most notable reduction of rainfall is found to the west of the rainfall center, i.e., ahead of the Taihang Mountains, which can exceed 12 mm (Fig. 9). Thus, the spurious rainfall near 116°E in EXP_KD05 is significantly alleviated in EXP_X21.

Figure 9 displays the differences between the horizontal winds at 925 hPa in experiments EXP_KD05 and EXP_X21. Herein, the wind fields are also smoothed using the two-dimensional FFT to remove disturbances of horizontal scales less than 150 km as in Fig. 7a. (The unsmoothed wind fields can be found in appendix B.) In general, the wind differences show a cyclonic circulation, with downslope flow over the

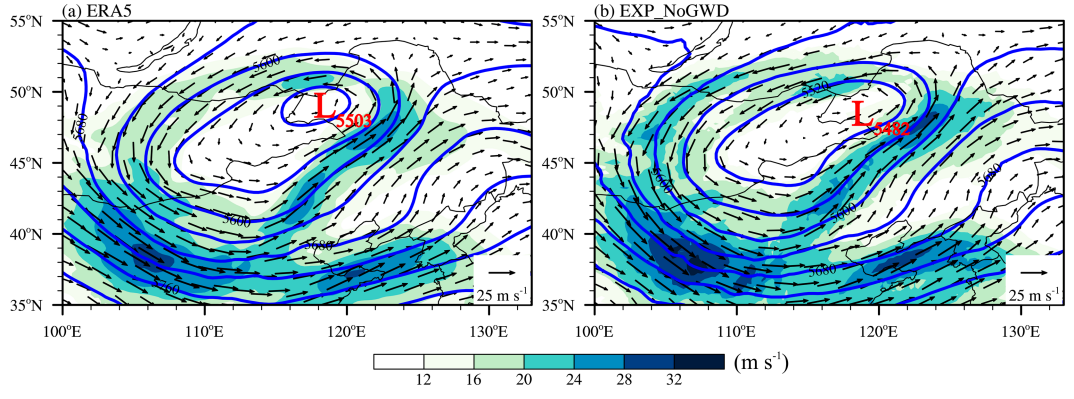

FIG. 5. GPH (contour at an interval of 40 gpm; gpm) and horizontal wind (vector) and its speed (shaded; m s^{-1}) at 500 hPa averaged between 1800 UTC 6 Jul 2011 and 0000 UTC 7 Jul 2011 from the (a) ERA5 reanalysis and (b) EXP_NoGWD experiment.

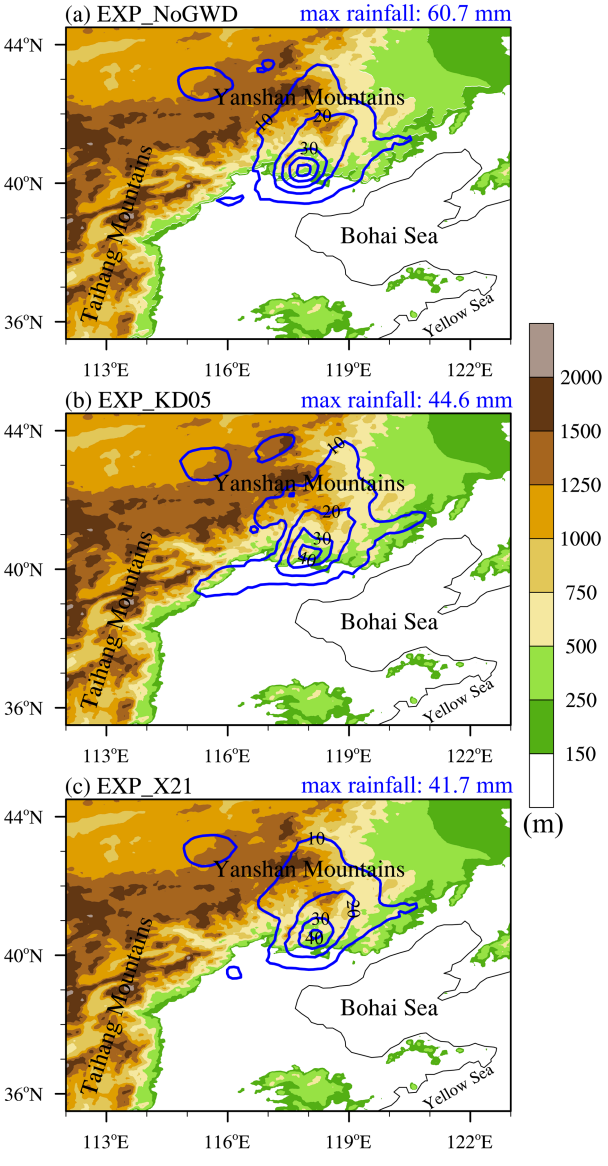

FIG. 6. Geographic distribution of the 6-h accumulative precipitation (contours at an interval of 10 mm; mm) during the period of 1800 UTC 6 Jul 2011–0000 UTC 7 Jul 2011 and model resolved orography (shaded; m) obtained from the experiments of (a) EXP_NoGWD, (b) EXP_KD05, and (c) EXP_X21, with the maximum rainfall value labeled in the top-right corner of each subplot. Note that the thin black solid lines near the Bohai Sea indicate the coastline.

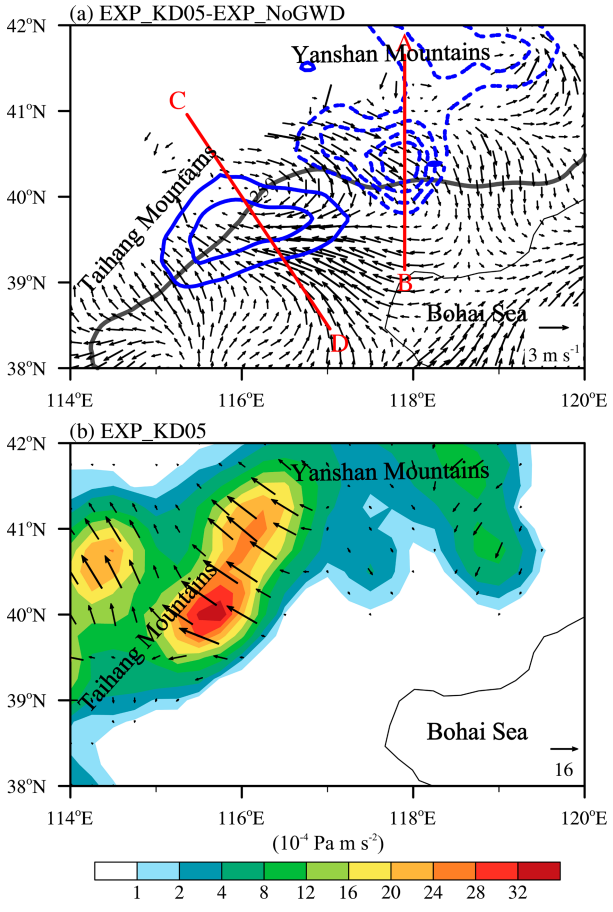

FIG. 7. (a) Differences between the 925-hPa horizontal winds (vectors; m s^{-1}) at 1800 UTC 6 Jul 2011 and the 6-h accumulated precipitation (contoured at an interval of 4 mm with negative values dashed and zero values omitted; mm) in experiments EXP_KD05 and EXP_NoGWD. The horizontal winds are smoothed using the two-dimensional FFT to remove disturbances of horizontal scales less than 150 km. The thick gray line marks the terrain elevation of 250 m, and red lines AB and CD indicate the locations of the vertical cross sections shown in Fig. 8. (b) Column-integrated OGWD (vector) and its magnitude (shading; 10^{-4} Pa m s^{-2}) in the experiment of EXP_KD05 at 1800 UTC 6 Jul 2011.

southeastern slope of the Taihang Mountains and upslope flow over the southern slope of the Yanshan Mountains, i.e., just opposite to that in Fig. 7a. It suggests that the NECV in EXP_X21 is enhanced than in EXP_KD05. (Note that the model biases are obtained by comparison with the ERA5 reanalysis.) This is clearly shown in Fig. 10 which illustrates the vertical distributions of biases in NECV intensity. As in Xu et al. (2023a), the NECV intensity is represented by the mean GPH averaged within 1° × 1° box centered at the GPH minimum of the NECV. In the absence of OGWD parameterization, the GPH of the NECV is underestimated by −17.7 gpm (averaged in the layer of 800–300 hPa), i.e., NECV is too strong, especially in the lower troposphere. These biases are overcorrected in EXP_KD05, showing a positive GPH bias of 21.5 gpm on average. The revised OGWD scheme can effectively mitigate this issue, reducing the GPH bias by about 50%, which is only 12.0 gpm. Correspondingly, the horizontal winds in EXP_X21 are enhanced compared to that in EXP_KD05 under the constraint of geostrophic balance.

In particular, the enhancement of the downslope winds over the Taihang Mountains is much stronger, which can exceed 3 m s^{-1}. This widespread downslope flow prevents the

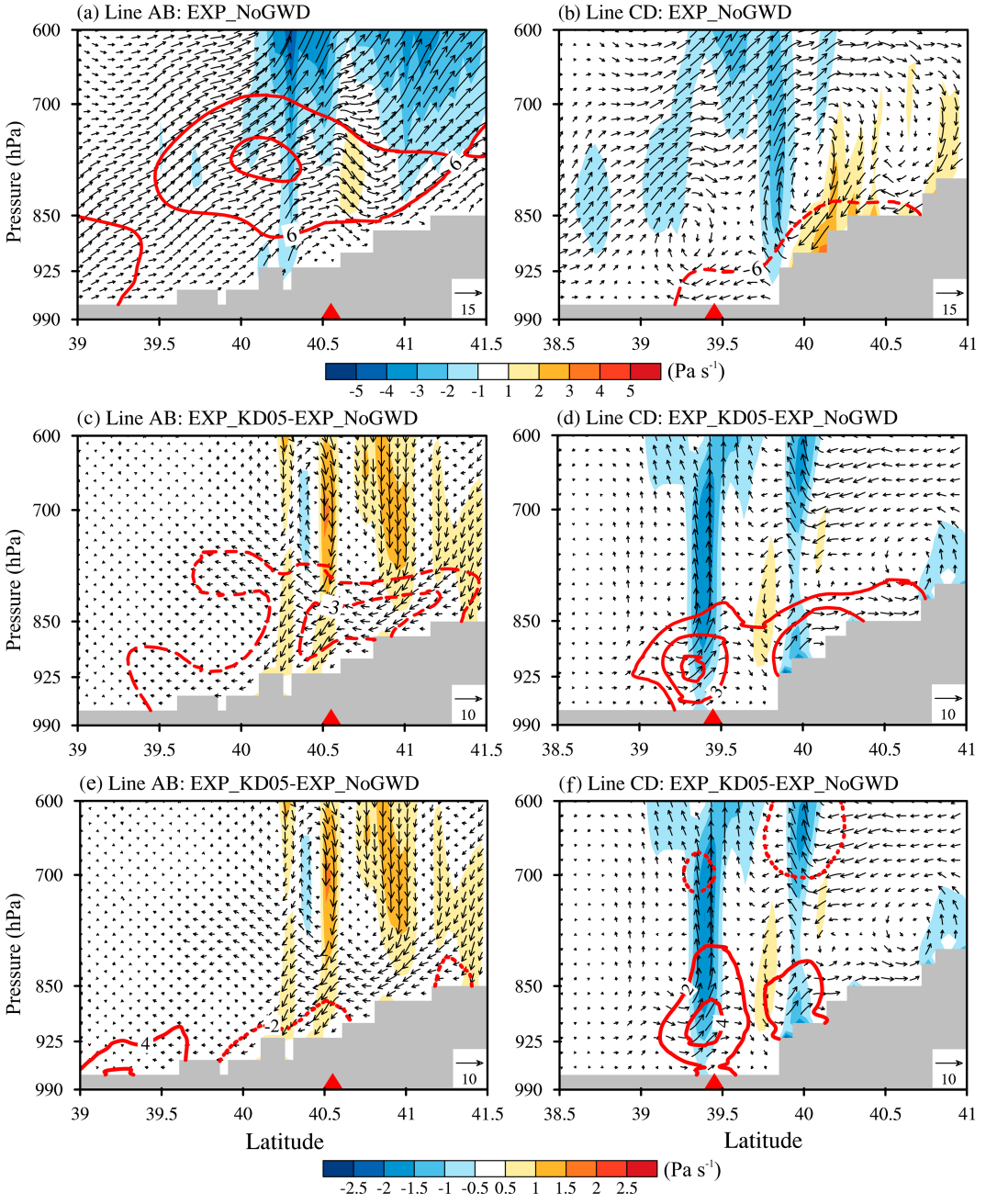

FIG. 8. Wind circulation (vectors; m s^{-1}; the vertical component is enlarged by 5 times for clarity), vertical velocity (shaded; Pa s^{-1}), and horizontal water vapor flux (contours at an interval of 3×10^{-2} kg m^{-1} s^{-1} Pa^{-1}) in the vertical planes of (a) line AB and (b) line CD in Fig. 7a in the experiment of EXP_NoGWD at 1800 UTC 6 Jul 2011. (c),(d) As in (a) and (b), but for the differences between the two experiments of EXP_KD05 and EXP_NoGWD, with the contours at an interval of 1.5×10^{-2} kg m^{-1} s^{-1} Pa^{-1}. Red triangle indicates the location of the rainfall center. Red solid and dashed contours indicate the horizontal water vapor flux vectors to the north and to the south, respectively, and gray shading indicates the region underground. (e),(f) As in (c) and (d), but with the contours for the equivalent potential temperature (contours at an interval of 2 K).

northward transport of the warm, moist air by the low-level southwesterly winds (Fig. 4d), leading to the pronounced reduction of rainfall ahead of the Taihang Mountains. The rainfall is also slightly reduced on the southern slope of the Yanshan Mountains, given the northwesterly winds near 118°E.

The differences in the wind circulation are due to the changes in parameterized OGWD. As shown in Fig. 11a, the

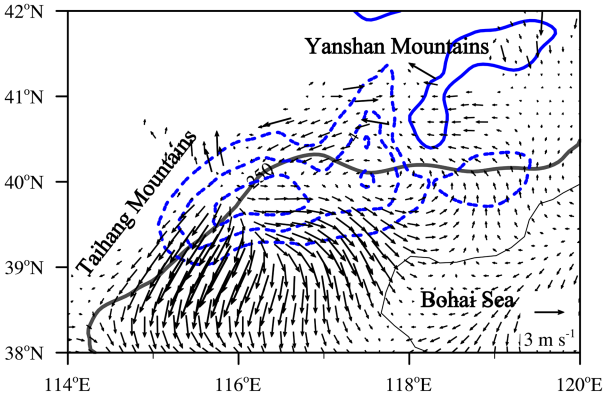

FIG. 9. Differences between the 925-hPa horizontal winds (vectors; m s^{-1}) at 1800 UTC 6 Jul 2011 and the 6-h accumulated precipitation (contoured at an interval of 4 mm with negative values dashed and zero values omitted; mm) in the two experiments of EXP_X21 and EXP_KD05. The horizontal winds are smoothed using the two-dimensional FFT to remove disturbances of horizontal scales less than 150 km. The thick gray line marks the terrain elevation of 250 m.

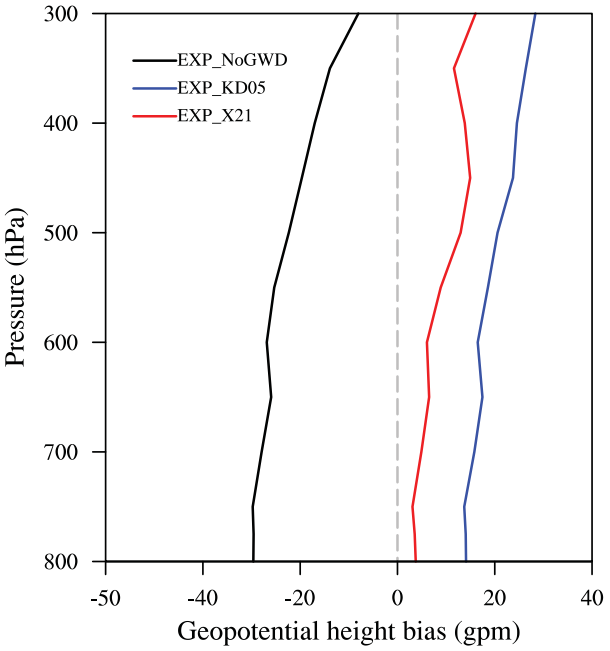

FIG. 10. Vertical distributions of GPH biases (gpm) with respect to the ERA5 reanalysis, averaged within a box of 1° × 1° centered at the NECV, obtained from the experiments of EXP_NoGWD, EXP_KD05, and EXP_X21 during the period of 1800 UTC 6 Jul 2011–0000 UTC 7 Jul 2011.

column-integrated OGWD in EXP_X21 becomes weaker after accounting for the NHE corrections. This is expected because the NHE acts to decrease the surface wave momentum flux of OGWs in theory (X21). The greatest reduction of the column-integrated OGWD is found over the Taihang Mountains, which is larger than 1.6×10^{-3} Pa m s^{-2}. In contrast, the OGWD is only weakly reduced over the Yanshan Mountains. This explains why the wind circulation differences mainly occur over the Taihang Mountains (Fig. 9).

To better understand the influence of the NHE on the OGWD, Fig. 11b shows the spatial distribution of the nondimensional horizontal Froude number (Fr) in experiment EXP_X21, i.e.,

$$\mathrm{Fr} = \frac{|\mathbf{V}_L|}{N_L L_x}, \tag{1}$$

where $\mathbf{V}_L$ is the low-level mean flow obtained by averaging the horizontal winds between the surface and $2\sigma_h$ above the surface (σ_h denotes the standard deviation of the SSO height), N_L is the mean buoyancy frequency obtained in a similar manner to that of $\mathbf{V}_L$, and L_x is the effective SSO length along the direction of $\mathbf{V}_L$. As revealed in X21, Fr measures the degree of nonhydrostaticity of OGWs, with the NHE correction given by

$$\mathrm{NHE(Fr)} = -\frac{9}{8}\mathrm{Fr}^2 + e^{-2\mathrm{Fr}^{-1}}\left(-\frac{5}{4}\mathrm{Fr}^{-2} - \frac{1}{2}\mathrm{Fr}^{-1} + \frac{5}{4} + \frac{9}{4}\mathrm{Fr} + \frac{9}{8}\mathrm{Fr}^2\right). \tag{2}$$

Note that Eq. (2) denotes the portion of the surface wave momentum flux of OGWs (which is equal to the column-integrated OGWD) weakened by the nonhydrostatic effect. Therefore, the actual decrease of OGWD also depends on its magnitude. In the regions of complex terrain, the horizontal Froude number can exceed 1.0, in particular over the Yanshan Mountains where Fr is greater than 2.5 (Fig. 11b). Theoretically, the OGWD will be reduced by more than −80%, indicating very marked NHE there (Fig. 11c). However, as shown in Fig. 11a, the reduction of the OGWD is more notable over the Taihang Mountains than over Yanshan Mountains. As mentioned above, this is owing to that the OGWD itself is much stronger over the Taihang Mountains, given the higher SSO there (Fig. 1b).

5. Summary and discussion

This work explores the impacts of orographic gravity wave drag (OGWD) on a heavy rainfall event which occurred in the night and early morning of 7 July 2011, under the synoptic background of a Northeast China cold vortex (NECV). The heavy rainfall center occurred on the southern slope of the Yanshan Mountains in North China, with the 6-h accumulated rainfall reaching about 50 mm. This short-term intense rainfall is simulated using the Weather Research and Forecasting (WRF) Model, with a grid spacing of 3 km. To investigate the impact of parameterized OGWD and a newly developed OGWD scheme including the nonhydrostatic effect (NHE) of OGWs, three numerical experiments are conducted. The first experiment (i.e., EXP_NoGWD) does not include the parameterization of OGWD, and the second experiment (i.e., EXP_KD05) uses the OGWD scheme of KD05. In the third experiment (i.e., EXP_X21), we use a modified version of the

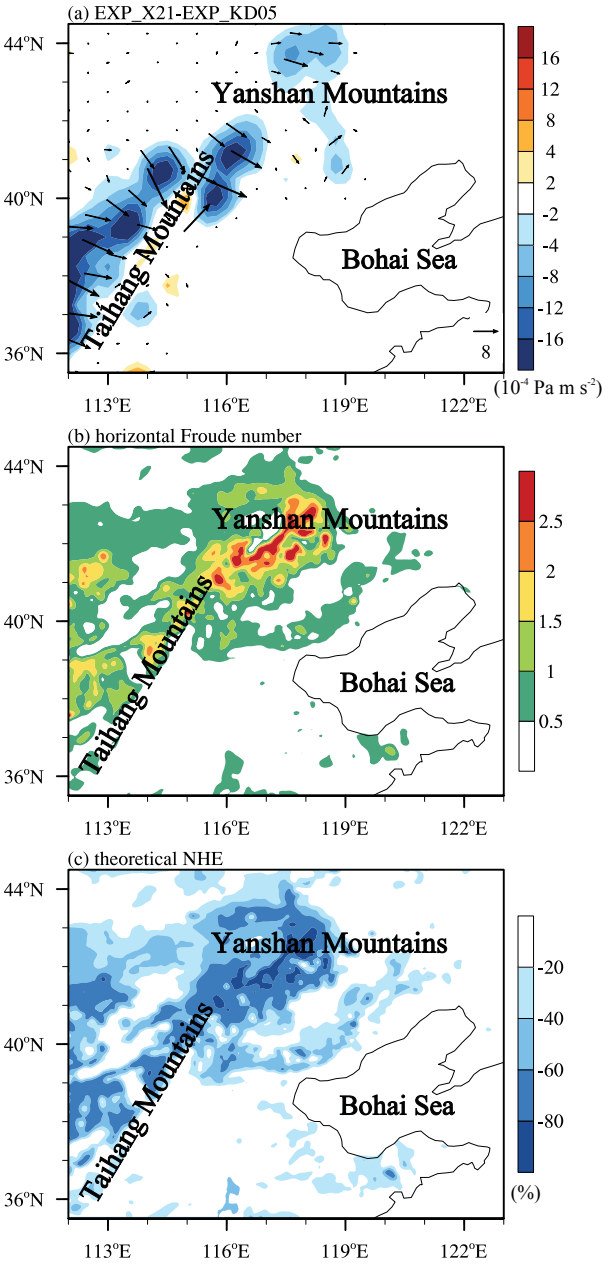

FIG. 11. (a) Difference in the column-integrated OGWD (vector) and its magnitude (shading; 10^{-4} Pa m s^{-2}) between the two experiments of EXP_X21 and EXP_KD05, (b) geographical distribution of the horizontal Froude number, and (c) theoretical NHE correction (%) in EXP_X21 experiment at 1800 UTC 6 Jul 2011.

KD05 scheme taking into account the NHE on the momentum flux of upward-propagating OGWs at the surface (X21).

Results show that the high-resolution WRF Model in general captures the location of the heavy rainfall on the southern slope of the Yanshan Mountains, even in the absence of OGWD parameterization (Fig. 12a). Yet, the intensity of the heavy rainfall is notably overestimated by about 27.5% in EXP_NoGWD. This intensity bias is obviously decreased when using the KD05 OGWD scheme in the WRF Model (i.e., EXP_KD05). However, it causes widespread spurious rainfall ahead of the Taihang Mountains. Further analysis reveals that the OGWD weakens the NECV cyclonic circulation. Thus, the upslope winds on the southern slope of the Yanshan Mountains are decreased, leading to a suppression of orographic lifting and moisture transport to the region of heavy rainfall. Meanwhile, the northwesterly flow downgliding the southeastern slope of the Taihang Mountains is also decelerated, which enhances the moisture transport toward the Taihang Mountains and produces excessive rainfall (Fig. 12b).

When accounting for the NHE in the OGWD parameterization, i.e., EXP_X21, the WRF Model slightly degrades the simulation of the heavy rainfall intensity, as compared to EXP_KD05. Nonetheless, the spurious rainfall ahead of the Taihang Mountains is removed entirely. This is owing to the fact that the NHE corrections act to weaken the OGWD and thus enhance the NECV circulation, in particular over the Taihang Mountains where the underlying terrain is more complex than the Yanshan Mountains. The downslope winds on the southeastern slope and at the foot of the Taihang Mountains are significantly enhanced, which acts to prevent the moisture transport toward the terrain. Spurious precipitation is thus inhibited.

To sum up, this study provides an insight into the impacts of complex terrain on the heavy rainfall under the background of NECV, from the viewpoint of OGWs and their drag effect. The OGWD can notably affect the rainfall intensity and location by modifying the NECV circulation and its interaction with the topography including moisture transport and orographic lifting. The findings underscore the importance of OGWD parameterization for the prediction of rainfall in regions of complex terrain, even in high-resolution models where OGWD parameterization has long been thought to be unimportant. It is thus critical to accurately represent the OGWD in the model. The revised OGWD scheme by X21, which theoretically accounts for the NHE in constant flow, is shown to be beneficial to the simulation of rainfall in high-resolution models. The generation and propagation of OGWs are also notably affected by environmental conditions, e.g., the vertical shear and curvature of ambient wind. Previous studies showed that the variations of both wind direction and speed with height can influence the magnitude and vertical distribution of OGW momentum flux and its interaction with the mean flow (e.g., Shutts 1995; Teixeira et al. 2004; Miranda et al. 2009; Xu et al. 2012, 2013, 2018; Turner et al. 2019; Xu et al. 2020; van Niekerk et al. 2023; R. Zhang et al. 2025). Therefore, more sophisticated parameterization schemes for nonhydrostatic OGWs generated in sheared flow are needed to improve the representation of OGWD in weather and climate models.

This study also has some limitations. It only considers a heavy rainfall event produced by an NECV. More cases of heavy rainfall are still needed, probably in other mountainous regions (e.g., the Tibetan Plateau) produced by different weather systems, e.g., the Tibetan Plateau vortex and southwest vortex (Fu et al. 2019; Li and Zhang 2023). Actually, we are examining a heavy rainfall event in Sichuan Basin, Southwest China, using 3-km resolution WRF simulations. In spite

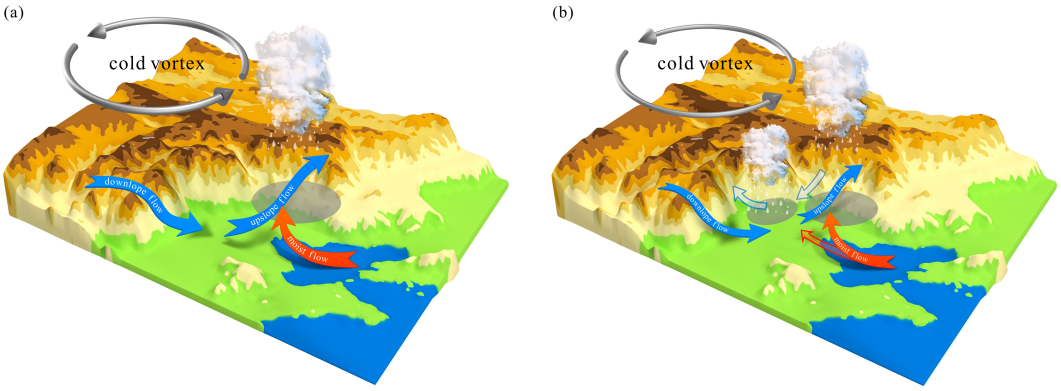

FIG. 12. (a) Schematic diagram for the dynamical processes of the heavy rainfall in EXP_NoGWD. The midlevel NECV is denoted by gray cyclonic arrow, while its near-surface cyclonic circulation that goes downslope and upslope of the Taihang and Yanshan Mountains is represented by blue solid arrows. Red solid arrow indicates the low-level moist flow from the Bohai Sea. (b) As in (a), but for the EXP_KD05 experiment. The gray cyclonic arrow is thinner than in (a), indicating an overall weakening of the NECV by the OGWD. The blue solid arrows are also smaller than in (a), with the blue empty arrows denoting the OGWD-induced circulation difference near the surface. Similarly, the red empty arrow represents the difference of low-level moisture transport, which is toward the Taihang Mountains, leading to spurious rainfall there.

of the different complex terrains in Southwest and Northeast China, the parameterization of OGWD is also found to help improve the simulation of heavy rainfall intensity and distribution in the high-resolution model, which will be shown in a companion paper. Moreover, the present study focuses on the effect of OGWD only. The effect of turbulent orographic form drag (TOFD), which is caused by fine-scale terrain narrower than roughly 5 km (e.g., Beljaars et al. 2004; Sandu et al. 2019), is not considered herein because our previous study (Xu et al. 2023a) showed a weak influence of TOFD on this NECV case. Nevertheless, past studies have emphasized the importance of TOFD in improving the simulation of precipitation in complex terrain regions in high-resolution models (Wang et al. 2020; Xue et al. 2021; J. Li et al. 2024; Q. Zhang et al. 2025). Therefore, it is interesting to investigate the joint effects of OGWD and TOFD in simulations of rainfall in high-resolution models in the future.

Acknowledgments. This work is mainly supported by the National Key Research and Development Program of China (Grant 2023YFC3007502), the Guangdong Province Meteorology Joint Fund (2024A1515510010), and the Fundamental Research Funds for the Central Universities (Grant 14380222).

Data availability statement. All data used for the analysis and analytical model development are available in the public domain. The ERA5 data are available at https://doi.org/10.24381/cds.bd0915c6 (Hersbach et al. 2018). The 0.1° gridded half hourly precipitation IMERG data are available at https://doi.org/10.5067/GPM/IMERG/3B-HH/07 (Huffman et al. 2023). The WRF Model outputs have been uploaded to https://doi.org/10.6084/m9.figshare.28426628.v2.

APPENDIX A

The Parameterization of OGWD in the WRF Model

The WRF Model adopts the OGWD parameterization scheme developed by KD05. In this scheme, the wave stress at the reference level is expressed as

$$\tau_0 = \rho_0 E \frac{m}{\lambda_{\text{eff}}} G \frac{|\mathbf{V}_L|^3}{N_L}, \tag{A1}$$

where

$$E = (\text{OA} + 2)^{C_E(\text{Fr}_0/\text{Fr}_c)}, \; m = (1 + L_x)^{\text{OA}+1},$$
$$G = \frac{\text{Fr}_0^2}{\text{Fr}_0^2 + C_G \text{OC}^{-1}}, \; \text{Fr}_0 = \frac{2\sigma_h N_L}{|\mathbf{V}_L|}\text{OD}. \tag{A2}$$

The "number of mountains" within the model grid cell (i.e., m) is used to measure the bulk volume of the SSO. The factor λ_{eff} is a tunable coefficient indicating the effective grid length, which is practically set to be 3 times the grid spacing of the model. The coefficient E denotes the drag enhancement by low-level wave breaking and/or lee wave trapping subject to the shape and location of the SSO within the grid cell and the flow nonlinearity measured by the nondimensional mountain height Fr_0. According to the criterion of $\text{Fr}_c = 1$, the coefficient G provides a transition between flow blocking and nonblocking. The $C_E = 0.8$ and $C_G = 0.5$ are the two constants empirically calibrated using numerical simulations (Kim and Arakawa 1995). Several features of the SSO are considered. The σ_h denotes the standard deviation of the SSO height, and L_x is the effective SSO length along the direction of low-level mean flow $\mathbf{V}_L$ obtained by averaging the horizontal winds below $2\sigma_h$ above the surface. The nondimensional parameters OA, OC,

and OD measure the asymmetry, sharpness, and anisotropy of the SSO, respectively.

According to the wave saturation hypothesis (Lindzen 1981), freely propagating OGWs are considered to break and deposit their wave momentum into the mean flow when the minimum Richardson number Ri_m falls below a critical value of $\mathrm{Ri}_c = 0.25$. Readers are referred to KD05 for more details about the scheme.

In both Xu et al. (2024) and M. Li et al. (2024), the KD05 scheme was revised by accounting for the NHE on the reference-level wave stress based on the theoretical solution derived in X21, i.e.,

$$\widetilde{\tau}_0 = \tau_0[1 + \mathrm{NHE}(\mathrm{Fr})], \tag{A3}$$

where

$$\mathrm{NHE}(\mathrm{Fr}) = -\frac{9}{8}\mathrm{Fr}^2 + e^{-2\mathrm{Fr}^{-1}}\left(-\frac{5}{4}\mathrm{Fr}^{-2} - \frac{1}{2}\mathrm{Fr}^{-1} + \frac{5}{4} + \frac{9}{4}\mathrm{Fr} + \frac{9}{8}\mathrm{Fr}^2\right). \tag{A4}$$

The NHE depends on the horizontal Froude number given by

$$\mathrm{Fr} = \frac{|\mathbf{V}_L|}{N_L L_x}, \tag{A5}$$

with N_L being the mean buoyancy frequency obtained in a similar manner to that of $\mathbf{V}_L$. The NHE correction is always negative, implying a decrease in the wave stress. Readers are referred to X21 and Xu et al. (2024) for more details about the NHE and the revision of the KD05 scheme.

APPENDIX B

WRF Model Output without Smoothing

Figures 7a and 9 display the differences between the 925-hPa wind circulations in different numerical experiments which are smoothed using two-dimensional FFT. Their unsmoothed counterparts are shown in Fig. B1.

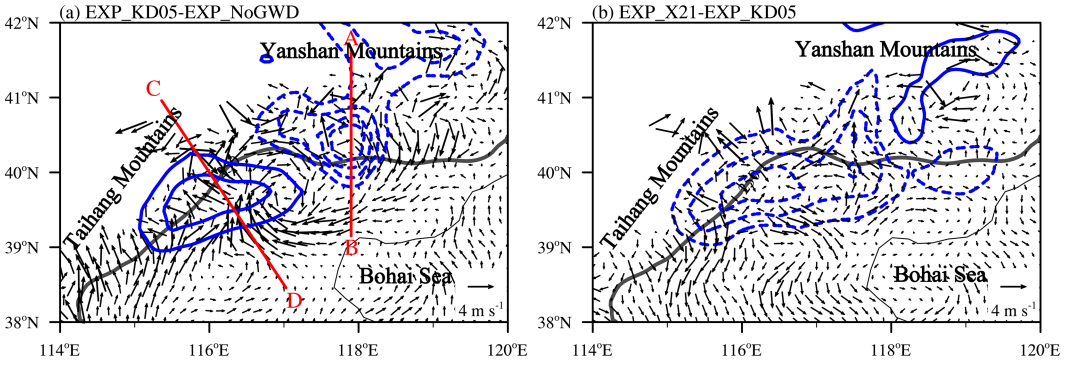

FIG. B1. Differences between the 925-hPa horizontal winds (vectors; m s^{-1}) at 1800 UTC 6 Jul 2011 and the 6-h accumulated precipitation (contoured at an interval of 4 mm with negative values dashed and zero values omitted; mm) in the two experiments of (a) EXP_KD05 and EXP_NoGWD and (b) EXP_X21 and EXP_KD05. The thick gray line marks the terrain elevation of 250 m.

REFERENCES

Beljaars, A. C. M., 1995: The parametrization of surface fluxes in large-scale models under free convection. *Quart. J. Roy. Meteor. Soc.*, **121**, 255–270, https://doi.org/10.1002/qj.49712152203.

——, A. R. Brown, and N. Wood, 2004: A new parametrization of turbulent orographic form drag. *Quart. J. Roy. Meteor. Soc.*, **130**, 1327–1347, https://doi.org/10.1256/qj.03.73.

Chen, X., X. Zhuge, X. Zhang, X. Zhang, Y. Wang, and D. Xue, 2023: Objective identification and climatic characteristics of heavy-precipitation northeastern China cold vortexes. *Adv. Atmos. Sci.*, **40**, 305–316, https://doi.org/10.1007/s00376-022-2037-y.

Du, Y., F. Zhang, Y. Q. Sun, J. Wei, and X. Li, 2021: Practical and intrinsic predictability of wave-convection coupled bands over southern China. *J. Geophys. Res. Atmos.*, **126**, e2021JD034882, https://doi.org/10.1029/2021JD034882.

Fan, Z., M. Xue, K. Zhu, H. Wang, and D. Yao, 2024: Initiation of prefrontal convection within a northeast China cold vortex: The roles of elevated front and dry air intrusion. *Quart. J. Roy. Meteor. Soc.*, **150**, 5284–5304, https://doi.org/10.1002/qj.4870.

Fu, S.-M., Z. Mai, J.-H. Sun, W.-L. Li, Y. Ding, and Y.-Q. Wang, 2019: Impacts of convective activity over the Tibetan Plateau on plateau vortex, southwest vortex, and downstream precipitation. *J. Atmos. Sci.*, **76**, 3803–3830, https://doi.org/10.1175/JAS-D-18-0331.1.

Hersbach, H., and Coauthors, 2018: ERA5 hourly data on pressure levels from 1959 to present. Copernicus Climate Change Service (C3S) Climate Data Store (CDS), accessed 6 July 2011, https://doi.org/10.24381/cds.bd0915c6.

Hong, S.-Y., Y. Noh, and J. Dudhia, 2006: A new vertical diffusion package with an explicit treatment of entrainment processes. *Mon. Wea. Rev.*, **134**, 2318–2341, https://doi.org/10.1175/MWR3199.1.

Houze, R. A., Jr., 2012: Orographic effects on precipitating clouds. *Rev. Geophys.*, **50**, RG1001, https://doi.org/10.1029/2011RG000365.

Hu, K., R. Lu, and D. Wang, 2010: Seasonal climatology of cutoff lows and associated precipitation patterns over northeast China. *Meteor. Atmos. Phys.*, **106**, 37–48, https://doi.org/10.1007/s00703-009-0049-0.

Hua, S., X. Xu, and B. Chen, 2020: Influence of multiscale orography on the initiation and maintenance of a precipitating convective system in North China: A case study. *J. Geophys. Res. Atmos.*, **125**, e2019JD031731, https://doi.org/10.1029/2019JD031731.

Huffman, G., E. Stocker, D. Bolvin, E. Nelkin, and T. Jackson, 2023: GPM IMERG final precipitation L3 half hourly 0.1 degree x 0.1 degree V07 (GPM_3IMERGHH). Goddard Earth Sciences Data and Information Services Center (GES DISC), accessed 6 July 2011, https://doi.org/10.5067/GPM/IMERG/3B-HH/07.

Iacono, M. J., J. S. Delamere, E. J. Mlawer, M. W. Shephard, S. A. Clough, and W. D. Collins, 2008: Radiative forcing by long-lived greenhouse gases: Calculations with the AER radiative transfer models. *J. Geophys. Res.*, **113**, D13103, https://doi.org/10.1029/2008JD009944.

Kim, Y.-J., 2007: Balance of drag between the middle and lower atmospheres in a global atmospheric forecast model. *J. Geophys. Res.*, **112**, D131404, https://doi.org/10.1029/2007JD008647.

——, and A. Arakawa, 1995: Improvement of orographic gravity wave parameterization using a mesoscale gravity wave model. *J. Atmos. Sci.*, **52**, 1875–1902, https://doi.org/10.1175/1520-0469(1995)052<1875:IOOGWP>2.0.CO;2.

——, and J. D. Doyle, 2005: Extension of an orographic-drag parametrization scheme to incorporate orographic anisotropy and flow blocking. *Quart. J. Roy. Meteor. Soc.*, **131**, 1893–1921, https://doi.org/10.1256/qj.04.160.

——, S. D. Eckermann, and H. Y. Chun, 2003: An overview of the past, present and future of gravity-wave drag parametrization for numerical climate and weather prediction models. *Atmos.–Ocean*, **41**, 65–98, https://doi.org/10.3137/ao.410105.

Kruse, C. G., and Coauthors, 2022: Observed and modeled mountain waves from the surface to the mesosphere near the Drake Passage. *J. Atmos. Sci.*, **79**, 909–932, https://doi.org/10.1175/JAS-D-21-0252.1.

Li, J., and Coauthors, 2024: The influence of complex terrain on cloud and precipitation on the foot and slope of the southeastern Tibetan Plateau. *Climate Dyn.*, **62**, 3143–3163, https://doi.org/10.1007/s00382-023-07056-3.

Li, L., and R. Zhang, 2023: Interdecadal shift in dipole pattern precipitation trends over the Tibetan Plateau: Roles of local vortices. *Geophys. Res. Lett.*, **50**, e2022GL101445, https://doi.org/10.1029/2022GL101445.

Li, M., X. Xu, M. A. C. Teixeira, M. Xue, H. Xue, K. Zhu, and H. Huang, 2024: Improved orographic gravity wave drag parameterization accounting for the nonhydrostatic effect in the weather research and forecasting model: Tests for short-range forecast of northeast China cold vortices. *Mon. Wea. Rev.*, **152**, 2623–2637, https://doi.org/10.1175/MWR-D-24-0097.1.

Li, N., B. Jiao, L. Ran, X. Shen, and Y. Qi, 2021: On the mechanism of a terrain-influenced snow burst event during midwinter in northeast China. *Adv. Atmos. Sci.*, **38**, 800–816, https://doi.org/10.1007/s00376-020-0104-9.

Li, R., X. Xu, X. Xu, T. G. Shepherd, and Y. Wang, 2023: Importance of orographic gravity waves over the Tibetan Plateau on the spring rainfall in East Asia. *Sci. China Earth Sci.*, **66**, 2594–2602, https://doi.org/10.1007/s11430-023-1204-6.

Lindzen, R. S., 1981: Turbulence and stress owing to gravity wave and tidal breakdown. *J. Geophys. Res.*, **86**, 9707–9714, https://doi.org/10.1029/JC086iC10p09707.

Liu, N., and C. Liu, 2018: Synoptic environments and characteristics of convection reaching the tropopause over northeast China. *Mon. Wea. Rev.*, **146**, 745–759, https://doi.org/10.1175/MWR-D-17-0245.1.

Liu, Y., Z. Liang, and Y. Li, 2017: Observational and simulative study of a local severe precipitation event caused by a cold vortex over northeast China. *Adv. Meteor.*, **2017**, 2764340, https://doi.org/10.1155/2017/2764340.

——, A. Xiao, F. Zhang, L. Zhang, and L. Liao, 2024: Analysis of precipitation zone forecasts and examination of numerical forecasts for two heavy rainfall processes in June 2019 in Jiangxi, China 2019. *Atmosphere*, **15**, 137, https://doi.org/10.3390/atmos15010137.

Lott, F., and M. J. Miller, 1997: A new subgrid-scale orographic drag parametrization: Its formulation and testing. *Quart. J. Roy. Meteor. Soc.*, **123**, 101–127, https://doi.org/10.1002/qj.49712353704.

Luo, Y., and Coauthors, 2020: Science and prediction of heavy rainfall over China: Research progress since the reform and opening-up of new China. *J. Meteor. Res.*, **34**, 427–459, https://doi.org/10.1007/s13351-020-0006-x.

McLandress, C., T. G. Shepherd, S. Polavarapu, and S. R. Beagley, 2012: Is missing orographic gravity wave drag near 60°S the cause of the stratospheric zonal wind biases in chemistry–

climate models? *J. Atmos. Sci.*, **69**, 802–818, https://doi.org/10.1175/JAS-D-11-0159.1.

Meng, Z., and Coauthors, 2018: The deadliest tornado (EF4) in the past 40 years in China. *Wea. Forecasting*, **33**, 693–713, https://doi.org/10.1175/WAF-D-17-0085.1.

Miranda, P. M. A., J. P. A. Martins, and M. A. C. Teixeira, 2009: Assessing wind profile effects on the global atmospheric torque. *Quart. J. Roy. Meteor. Soc.*, **135**, 807–814, https://doi.org/10.1002/qj.393.

Nieto, R., and Coauthors, 2005: Climatological features of cutoff low systems in the Northern Hemisphere. *J. Climate*, **18**, 3085–3103, https://doi.org/10.1175/JCLI3386.1.

Sandu, I., P. Bechtold, A. Beljaars, A. Bozzo, F. Pithan, T. G. Shepherd, and A. Zadra, 2016: Impacts of parameterized orographic drag on the Northern Hemisphere winter circulation. *J. Adv. Model. Earth Syst.*, **8**, 196–211, https://doi.org/10.1002/2015MS000564.

——, and Coauthors, 2019: Impacts of orography on large-scale atmospheric circulation. *npj Climate Atmos. Sci.*, **2**, 10, https://doi.org/10.1038/s41612-019-0065-9.

Shutts, G., 1995: Gravity-wave drag parametrization over complex terrain: The effect of critical-level absorption in directional wind-shear. *Quart. J. Roy. Meteor. Soc.*, **121**, 1005–1021, https://doi.org/10.1002/qj.49712152504.

Skamarock, C., and Coauthors, 2019: A description of the Advanced Research WRF Model version 4. NCAR Tech. Note NCAR/TN-556+STR, 145 pp., https://doi.org/10.5065/1dfh-6p97.

Skamarock, W. C., J. B. Klemp, M. G. Duda, L. D. Fowler, S.-H. Park, and T. D. Ringler, 2012: A multiscale nonhydrostatic atmospheric model using centroidal Voronoi tesselations and C-grid staggering. *Mon. Wea. Rev.*, **140**, 3090–3105, https://doi.org/10.1175/MWR-D-11-00215.1.

Smith, R. B., 1979: The influence of the Earth's rotation on mountain wave drag. *J. Atmos. Sci.*, **36**, 177–180, https://doi.org/10.1175/1520-0469(1979)036<0177:TIOTER>2.0.CO;2.

——, 1980: Linear theory of stratified hydrostatic flow past an isolated mountain. *Tellus*, **32** (4), 348–364, https://doi.org/10.1111/j.2153-3490.1980.tb00962.x.

Sun, L., 1997: A study of the persistence activity of northeast cold vortex in China (in Chinese). *Chin. J. Atmos. Sci.*, **21**, 297–307.

Teixeira, M. A. C., 2014: The physics of orographic gravity wave drag. *Front. Phys.*, **2**, 43, https://doi.org/10.3389/fphy.2014.00043.

——, P. M. A. Miranda, and M. A. Valente, 2004: An analytical model of mountain wave drag for wind profiles withShear and curvature. *J. Atmos. Sci.*, **61**, 1040–1054, https://doi.org/10.1175/1520-0469(2004)061<1040:AAMOMW>2.0.CO;2.

Tewari, M., and Coauthors, 2004: Implementation and verification of the unified Noah land-surface model in the WRF model. *20th Conf. on Weather Analysis and Forecasting/16th Conf. on Numerical Weather Prediction*, Seattle, WA, Amer. Meteor. Soc., 11–15, https://n2t.net/ark:/85065/d7fb523p.

Thompson, G., P. R. Field, R. M. Rasmussen, and W. D. Hall, 2008: Explicit forecasts of winter precipitation using an improved bulk microphysics scheme. Part II: Implementation of a new snow parameterization. *Mon. Wea. Rev.*, **136**, 5095–5115, https://doi.org/10.1175/2008MWR2387.1.

Turner, H., M. A. C. Teixeira, J. Methven, and S. B. Vosper, 2019: Sensitivity of the surface orographic gravity wave drag to vertical wind shear over Antarctica. *Quart. J. Roy. Meteor. Soc.*, **145**, 164–178, https://doi.org/10.1002/qj.3416.

van Niekerk, A., S. B. Vosper, and M. A. C. Teixeira, 2023: Accounting for the three-dimensional nature of mountain waves: Parametrising partial critical-level filtering. *Quart. J. Roy. Meteor. Soc.*, **149**, 515–536, https://doi.org/10.1002/qj.4421.

Wang, G., D.-L. Zhang, and J. Sun, 2021: A multiscale analysis of a nocturnal extreme rainfall event of 14 July 2017 in northeast China. *Mon. Wea. Rev.*, **149**, 173–187, https://doi.org/10.1175/MWR-D-20-0232.1.

Wang, Y., and Coauthors, 2020: Synergy of orographic drag parameterization and high resolution greatly reduces biases of WRF-simulated precipitation in central Himalaya. *Climate Dyn.*, **54**, 1729–1740, https://doi.org/10.1007/s00382-019-05080-w.

Wei, P., and Coauthors, 2023: On the key dynamical processes supporting the 21.7 Zhengzhou record-breaking hourly rainfall in China. *Adv. Atmos. Sci.*, **40**, 337–349, https://doi.org/10.1007/s00376-022-2061-y.

——, and Coauthors, 2025: Complex terrain causes global model prediction biases of 21.7 Zhengzhou extreme precipitation. *Sci. Bull.*, https://doi.org/10.1016/j.scib.2025.09.015, in press.

White, R. H., J. M. Wallace, and D. S. Battisti, 2021: Revisiting the role of mountains in the Northern Hemisphere winter atmospheric circulation. *J. Atmos. Sci.*, **78**, 2221–2235, https://doi.org/10.1175/JAS-D-20-0300.1.

Wu, X., and Coauthors, 2021: Contribution of the northeast cold vortex index and multiscale synergistic indices to extreme precipitation over northeast China. *Earth Space Sci.*, **8**, e2020EA001435, https://doi.org/10.1029/2020EA001435.

Xia, R., and D.-L. Zhang, 2019: An observational analysis of three extreme rainfall episodes of 19–20 July 2016 along the Taihang Mountains in North China. *Mon. Wea. Rev.*, **147**, 4199–4220, https://doi.org/10.1175/MWR-D-18-0402.1.

Xu, S.-Q., H. Gao, Y.-H. Fang, X.-Y. Yang, and S.-W. Zhao, 2023: Dominant role of cold vortices on the precipitation in northeast China still exists in midsummer. *Int. J. Climatol.*, **43**, 7119–7131, https://doi.org/10.1002/joc.8255.

Xu, X., Y. Wang, and M. Xue, 2012: Momentum flux and flux divergence of gravity waves in directional shear flows over three-dimensional mountains. *J. Atmos. Sci.*, **69**, 3733–3744, https://doi.org/10.1175/JAS-D-12-044.1.

——, M. Xue, and Y. Wang, 2013: Gravity wave momentum flux in directional shear flows over three-dimensional mountains: Linear and nonlinear numerical solutions as compared to linear analytical solutions. *J. Geophys. Res. Atmos.*, **118**, 7670–7681, https://doi.org/10.1002/jgrd.50471.

——, Y. Tang, Y. Wang, and M. Xue, 2018: Directional absorption of parameterized mountain waves and its influence on the wave momentum transport in the Northern Hemisphere. *J. Geophys. Res. Atmos.*, **123**, 2640–2654, https://doi.org/10.1002/2017JD027968.

——, M. A. C. Teixeira, M. Xue, Y. Lu, and J. Tang, 2020: Impacts of wind profile shear and curvature on the parameterized orographic gravity wave stress in the Weather Research and Forecasting Model. *Quart. J. Roy. Meteor. Soc.*, **146**, 3086–3100, https://doi.org/10.1002/qj.3828.

——, R. Li, M. A. C. Teixeira, and Y. Lu, 2021: On the momentum flux of vertically propagating orographic gravity waves excited in nonhydrostatic flow over three-dimensional orography. *J. Atmos. Sci.*, **78**, 1807–1822, https://doi.org/10.1175/JAS-D-20-0370.1.

——, M. Li, S. Zhong, and Y. Wang, 2023a: Impact of parameterized topographic drag on a simulated northeast China cold

vortex. *J. Geophys. Res. Atmos.*, **128**, e2022JD037664, https://doi.org/10.1029/2022JD037664.

——, and Coauthors, 2023b: Reducing winter precipitation biases over the western Tibetan Plateau in the Model for Prediction Across Scales (MPAS) with a revised parameterization of orographic gravity wave drag. *J. Geophys. Res. Atmos.*, **128**, e2023JD039123, https://doi.org/10.1029/2023JD039123.

——, and Coauthors, 2024: A parameterization scheme accounting for nonhydrostatic effects on the momentum flux of vertically propagating orographic gravity waves: Formulas and preliminary tests in the Model for Prediction Across Scales (MPAS). *J. Atmos. Sci.*, **81**, 805–817, https://doi.org/10.1175/JAS-D-23-0020.1.

Xue, H., X. Zhou, Y. Luo, and J. Yin, 2021: Impact of parameterizing the turbulent orographic form drag on convection-permitting simulations of winds and precipitation over South China during the 2019 pre-summer rainy season. *Atmos. Res.*, **263**, 105814, https://doi.org/10.1016/j.atmosres.2021.105814.

Xue, M., and A. J. Thorpe, 1991: A mesoscale numerical model using the nonhydrostatic pressure-based sigma-coordinate equations: Model experiments with dry mountain flows. *Mon. Wea. Rev.*, **119**, 1168–1185, https://doi.org/10.1175/1520-0493(1991)119<1168:AMNMUT>2.0.CO;2.

Yang, L., and Y. Zheng, 2024: The short-duration heavy rainfall in different quadrants of northeast China cold vortices. *J. Meteor. Res.*, **38**, 321–338, https://doi.org/10.1007/s13351-024-3055-8.

Yin, L., F. Ping, H. Xu, and B. Chen, 2021: Numerical simulation and the underlying mechanism of a severe hail-producing convective system in East China. *J. Geophys. Res. Atmos.*, **126**, e2019JD032285, https://doi.org/10.1029/2019JD032285.

Zhang, C., Q. Zhang, Y. Wang, and X. Liang, 2008: Climatology of warm season cold vortices in East Asia: 1979–2005. *Meteor. Atmos. Phys.*, **100**, 291–301, https://doi.org/10.1007/s00703-008-0310-y.

Zhang, D.-L., Y. Lin, P. Zhao, X. Yu, S. Wang, H. Kang, and Y. Ding, 2013: The Beijing extreme rainfall of 21 July 2012: "Right results" but for wrong reasons. *Geophys. Res. Lett.*, **40**, 1426–1431, https://doi.org/10.1002/grl.50304.

Zhang, M., J. Li, N. Li, W. Sun, P. Li, and Y. Zhao, 2024: Spatial inhomogeneity of synoptic-induced precipitation in a region of steep topographic relief: A case study. *J. Geophys. Res. Atmos.*, **129**, e2023JD039129, https://doi.org/10.1029/2023JD039129.

Zhang, Q., and Coauthors, 2025: Integrating optimized cumulus and TOFD schemes for heavy precipitation forecasting in the Yarlung Tsangbo Grand Canyon. *Climate Dyn.*, **63**, 27, https://doi.org/10.1007/s00382-024-07503-9.

Zhang, R., X. Xu, and Y. Wang, 2020: Impacts of subgrid orographic drag on the summer monsoon circulation and precipitation in East Asia. *J. Geophys. Res. Atmos.*, **125**, e2019JD032337, https://doi.org/10.1029/2019JD032337.

——, Y. Lu, X. Xu, and Y. Wang, 2025: Impacts of wind profile shear and curvature on the parameterized orographic gravity wave stress in a middle atmosphere resolving general circulation model. *J. Adv. Model. Earth Syst.*, **17**, e2024MS004232, https://doi.org/10.1029/2024MS004232.

Zhao, S., and J. Sun, 2007: Study on cut-off low-pressure systems with floods over northeast Asia. *Meteor. Atmos. Phys.*, **96**, 159–180, https://doi.org/10.1007/s00703-006-0226-3.

Zheng, X. Y., T. Z. Zhang, and H. R. Bai, 1992: *Heavy Rainfall in Northeastern China (in Chinese)*. China Meteorological Press, 219 pp.

Zhong, L., R. Mu, D. Zhang, P. Zhao, Z. Zhang, and N. Wang, 2015: An observational analysis of warm-sector rainfall characteristics associated with the 21 July 2012 Beijing extreme rainfall event. *J. Geophys. Res. Atmos.*, **120**, 3274–3291, https://doi.org/10.1002/2014JD022686.

Zhou, X., A. Beljaars, Y. Wang, B. Huang, C. Lin, Y. Chen, and H. Wu, 2017: Evaluation of WRF simulations with different selections of subgrid orographic drag over the Tibetan Plateau. *J. Geophys. Res. Atmos.*, **122**, 9759–9772, https://doi.org/10.1002/2017JD027212.